AIP | Applied Physics Letters

Tunable bandgap in BiFeO3 nanoparticles: The role of microstrain and oxygen defects

Pavana S. V. Mocherla, C. Karthik, R. Ubic, M. S. Ramachandra Rao, and C. Sudakar

Citation: Appl. Phys. Lett. **103**, 022910 (2013); doi: 10.1063/1.4813539
View online: http://dx.doi.org/10.1063/1.4813539
View Table of Contents: http://apl.aip.org/resource/1/APPLAB/v103/i2
Published by the AIP Publishing LLC.

Tunable bandgap in $BiFeO_3$ nanoparticles: The role of microstrain and oxygen defects

Pavana S. V. Mocherla,[1] C. Karthik,[2] R. Ubic,[2] M. S. Ramachandra Rao,[3] and C. Sudakar[1,a)]

[1]*Multifunctional Materials Laboratory, Department of Physics, Indian Institute of Technology Madras, Chennai 600036, India*

[2]*Department of Materials Science and Engineering, Boise State University, 1910 University Drive, Boise, Idaho 83725, USA*

[3]*Department of Physics and Nano Functional Materials Technology Centre, Indian Institute of Technology Madras, Chennai 600036, India*

(Received 4 April 2013; accepted 20 June 2013; published online 12 July 2013)

We demonstrate a tunable bandgap from 2.32 eV to 2.09 eV in phase-pure $BiFeO_3$ by controlling the particle size from 65 nm to 5 nm. Defect states due to oxygen and microstrain show a strong dependence on $BiFeO_3$ particle size and have a significant effect on the shape of absorbance curves. Oxygen-defect induced microstrain and undercoordinated oxygen on the surface of $BiFeO_3$ nanoparticles are demonstrated via HRTEM and XPS studies. Microstrain in the lattice leads to the reduction in rhombohedral distortion of $BiFeO_3$ for particle sizes below 30 nm. The decrease in band gap with decreasing particle size is attributed to the competing effects of microstrain, oxygen defects, and Coulombic interactions. © *2013 AIP Publishing LLC*. [http://dx.doi.org/10.1063/1.4813539]

$BiFeO_3$ (BFO) is an extensively studied room-temperature multiferroic material with $T_N \sim 643$ K and $T_C \sim 1143$ K.[1–3] Various approaches to tune the magnetic and electrical properties of $BiFeO_3$ are being conducted to realize coupling between the ferroelectric and ferromagnetic order parameters at room temperature.[4–6] By controlling the crystallite size and defects, a significant tuning of the magnetic, electrical, and optical properties can be realized in $BiFeO_3$.[1,7,8] In recent years this material has been shown to be a promising candidate for photovoltaics[9,10] and photocatalysts.[11–13] Ferroelectric photovoltaic (FEPV) materials, which are both photosensitive and ferroelectric, present renewed interest in photoferroelectrics.[14,15] FEPV having large, above-bandgap photovoltage can offer high power conversion efficiencies. Polarization related charge separation mechanism leading to a significant increase in photovoltage due to the presence of electric field within the nanoscale domain walls has been demonstrated in $BiFeO_3$ thin films.[16,17] Therefore, engineering domain boundaries, local electric polarization, and bandgap of oxides are envisaged to bring in significant advancement in the field of FEPV. Understanding the electronic and defect structure of $BiFeO_3$ is essential in order to validate the suitability of the material in energy applications like these. Wang *et al.*[18] showed that the morphology and surface area are important factors that control the photocatalytic activity in $BiFeO_3$. The photoinduced oxidation ability of $BiFeO_3$ nanowires indicates that they can be used as photoelectrodes.[19] Multiferroic materials with small bandgaps are suitable candidates for optoelectronics and related device applications;[20] therefore, $BiFeO_3$, with a tunable bandgap will be appropriate for these applications. With the reduction in particle size, the bandgap of $BiFeO_3$ can be made to fall in the visible region, making it a potential photovoltaic material. The direct bandgap value of $BiFeO_3$ is 3.00 eV for single crystals[21] and 2.67 eV in thin films.[9] The bandgap has been shown to be influenced by the size and morphology of the crystallites in specific cases.[13] Several groups reported the bandgap of nanosized $BiFeO_3$ ranging from 2.18 eV to 2.3 eV (Refs. 5, 19, and 22); however, there are currently no reports which present a controlled tuning of bandgap with size.

In this report, the effect of crystallite size on optical properties of sol-gel synthesized single-crystalline $BiFeO_3$ nanoparticles is discussed, and a tunable bandgap varying from 2.32 eV to 2.09 eV is demonstrated. The effect of oxygen defects and microstrain on the optical properties is discussed as a function of crystallite size.

$BiFeO_3$ nanoparticles were prepared by a low-temperature citrate sol-gel process.[23] The resulting precursor gel was further dried into a powder by heating between 80 and 100 °C. The as-obtained dried precursor was calcined under controlled heating conditions at temperatures ranging from 350 °C to 550 °C. The crystallite size increases with increasing calcination temperature, and sizes ranging from 5 nm to 65 nm could be obtained by altering temperature and calcination time. Details of the calcination temperatures and durations as well as the corresponding labeling of the samples are given in Table I. Crystallite size was calculated from x-ray diffraction (XRD) using the Scherrer's formula for all the samples except for the sample calcined at 350 °C which was found to be x-ray amorphous (Fig. 1(a) and supplementary material (Fig. S1)[24]). For this sample, high-resolution transmission electron microscopy (HRTEM) images revealed local crystallization of $BiFeO_3$ resulting in ~5 nm crystalline nano-regions embedded in an amorphous phase. The calculated crystallite sizes of $BiFeO_3$ samples calcined at different temperatures are in good agreement with those observed in HRTEM images.

a)Author to whom correspondence should be addressed. Electronic mail: csudakar@iitm.ac.in. Tel.: +91-44-22574895.

TABLE I. Sample code, calcination temperature (T), calcination time (t), average crystallite size (d), bandgap (E_g), and lattice parameters (*a* and *c*) of BFO nanoparticles.

					Lattice parameters (Å)	
Sample code	T (±5 °C)	t (h)	d (nm)	E_g (eV)	*a*	*c*
BFO-5	350	3	~5	2.09	x-ray amorphous	
BFO-22	375	6	22	2.13	5.582	13.850
BFO-25	425	6	25	2.19	5.582	13.864
BFO-29	450	6	29	2.22	5.579	13.862
BFO-30	475	6	30	2.24	5.581	13.869
BFO-38	500	3	38	2.30	5.585	13.879
BFO-65	550	3	65	2.32	5.587	13.892

$BiFeO_3$ has a rhombohedrally distorted perovskite structure (space group *R*3*c*) with lattice parameters $a = 5.63$ Å and $\alpha = 59.35°$, but it is generally represented in the hexagonal setting with $a = 5.58$ Å and $c = 13.87$ Å.[8] Lattice parameters *a* and *c* were calculated by Rietveld refinement of XRD data using X'pert High Score software (Table I). The lattice parameter *a* does not show much change as a function of crystallite size; however, *c* decreases from 13.8919 Å for BFO-65 to 13.8498 Å for BFO-22. The *c*/*a* ratio as a function of crystallite size is plotted in Fig. 1(b). The decreasing trend in *c* with decreasing crystallite size has been reported by Selbach *et al.*,[8] who attributed it to the reduction in rhombohedral distortion of perovskite structure. This structural change is also evidenced from the reduced separation of (104) and (110) peak positions [$\Delta 2\theta_{(104)-(110)}$] (Fig. 1(a)), which would coalesce into a single (200) peak in the cubic phase. The microstrain as a function of crystallite size was also calculated from the XRD peak broadening (Fig. 1(c)). The symmetric broadening of the XRD peaks indicates that microscale internal strain varies from crystal to crystal.[25] The microstrain was found to be high for smaller crystallite sizes (<30 nm) and reduces with increase in size. The inverse relationship between microstrain and *c*/*a* ratio is noteworthy. The microstrain and lattice parameter variations represent lattice distortions which can arise from the grain boundaries present in nanocrystallites.[26] These particle size dependent structural details influence significantly the optical properties of $BiFeO_3$.

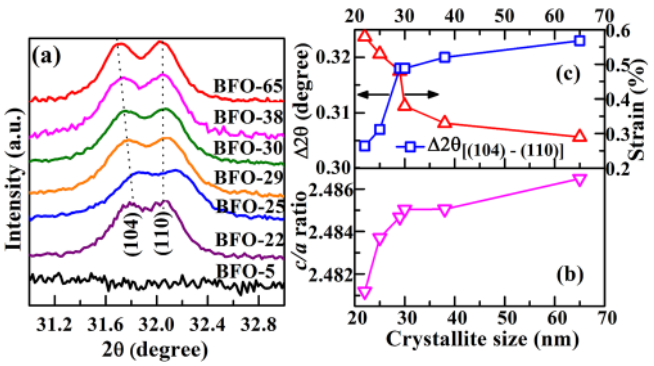

FIG. 1. (a) XRD patterns for different BFO samples (BFO-5 to BFO-65) showing the (104) and (110) reflections; (b) *c*/*a* ratio versus crystallite size of $BiFeO_3$ nanoparticles; (c) angular difference in (104) and (110) peak positions [$\Delta 2\theta_{(104)-(110)}$] and strain (%) of different $BiFeO_3$ nanoparticles are plotted as a function of crystallite size.

The particle size and microstructure of $BiFeO_3$ samples were examined via HRTEM using JEOL JEM-2100 HR operating at 200 kV. HRTEM micrographs with corresponding selected-area electron diffraction patterns (SADPs) are shown in Fig. 2. The microstructure of these samples with size distribution is given in Fig. S2 of supplementary material.[24] BFO-5 sample (Fig. 2(a)) does not show any microstructural features; however, this sample, which was found to be amorphous via XRD, appeared partially crystalline via electron diffraction. The SADP shows diffuse rings superimposed with spots (inset of Fig. 2(a)). The HRTEM image revealed the presence of small crystallites (marked with white circles in Fig. 2(a)) embedded in the amorphous phase. A magnified HRTEM image (inset of Fig. 2(a)) of a crystalline region reveals 2D lattice imaging with slightly distorted four-fold symmetry characteristic of $BiFeO_3$. As the calcination temperature increases the particles become well crystalline. For particles below 30 nm, the $BiFeO_3$ with reduced rhombohedral distortion is favored with different degrees of distortion within the same particle. This results in local tensile and compressive strains as discerned from the filtered lattice image obtained from FFT shown in Fig. 2(e) and supplementary material (Fig. S3).[24] This finding corroborates well with the large strain and small *c*/*a* ratio in BFO-22. For BFO-22, we observe well-faceted crystallites (Fig. 2(b)). As $BiFeO_3$ crystallizes from the amorphous phase, faceted growth takes place. These facets disappear as the particle size grows larger. For samples calcined at 500 °C (BFO-38) the average particle size was found to be around 40 nm, consistent with the crystallite size estimated via XRD. The SADP of these crystallites shows rings with superimposed

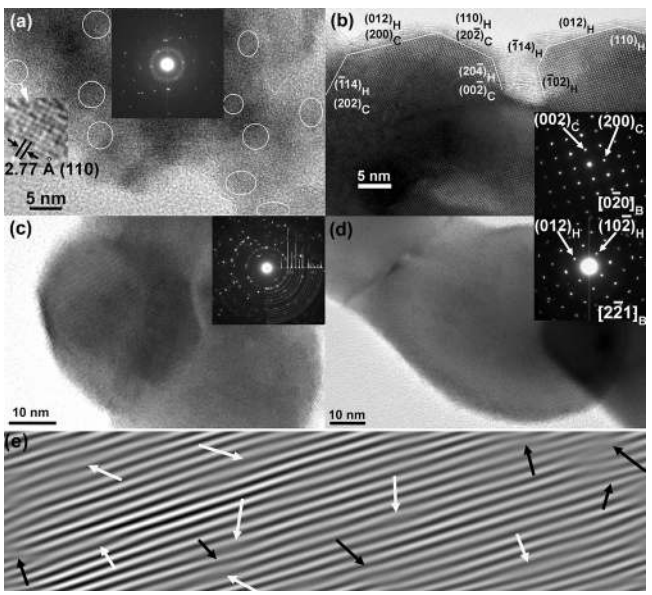

FIG. 2. HRTEM images and SADPs (insets) of (a) BFO-5, (b) BFO-22, (c) BFO-38, and (d) BFO-65 nanoparticles. Regions of local crystallization are marked by white circles in (a) and a magnified view of one such region with (110) lattice plane is marked. Facets of $BiFeO_3$ nanocrystals with pseudocubic symmetry (c) and trigonal symmetry with hexagonal indexing (H) are shown in (b). SADP in (c) is overlapped with simulated pattern. SADP in (b) and (d) are indexed with cubic and hexagonal (*h k l*) planes, respectively. (e) Filtered lattice image obtained from selectively masked FFT of a crystallite in (b) is shown. The white and black arrows show the regions of tensile and compressive strains, respectively.

spots indicating randomly oriented nanocrystallites (Fig. 2(c)). The overlapped simulated pattern confirms the $BiFeO_3$ phase. The HRTEM image in Fig. 2(c) shows three crystallites with different orientations and diffuse grain boundaries. When the sample is calcined to 550 °C (BFO-65), the particle size grows further to an average value ~65 nm. Individual particles are single crystalline and a typical SADP from one of the crystallites shows the $[2\bar{2}1]$ zone axis pattern of $BiFeO_3$ (inset of Fig. 2(d)). The HRTEM image shows two adjacent crystallites with the grain boundary still visible.

To find the valence state of Fe and metal-oxygen bonding characteristics in $BiFeO_3$ samples, x-ray photoelectron spectroscopy (XPS) was conducted. Fig. 3 shows the typical Fe 2p and O 1s XPS core spectra for BFO-5, BFO-38, and BFO-65 samples. Fe 2p spectra show the features mostly of Fe^{3+} oxidation state as discerned from the binding energy of Fe $2p_{3/2}$ (at 710.9 eV) for all the samples. In general, satellite peaks appear at 8 eV above $2p_{3/2}$ for Fe^{3+} and 6 eV above $2p_{3/2}$ for Fe^{2+}. In our samples, a satellite peak is seen ~7.5 eV above Fe $2p_{3/2}$, which further confirms the 3+ oxidation state of Fe. The O 1s spectra can be resolved into three peaks positioned around 529.6 eV, 530.8 eV, and 532.7 eV. In all the three samples the main peak due to O^{2-} in the lattice is at ~529.6 eV. In addition to this, a significantly intense O 1s peak at ~532.7 eV is observed in BFO-5 and BFO-38, which can be attributed to undercoordinated oxygen. The 532.7 eV O1s peak is more prominent in BFO-38, which suggests that there are a large number of surface oxygen defects in nanosized $BiFeO_3$ crystallites. In BFO-5 the relatively low intensity of this peak is due to the continuous amorphous phase embedded with $BiFeO_3$ nanoparticles. For BFO-65 the 532.7 eV O 1s peak is not seen, which indicates a significant reduction in surface oxygen defects. The Bi 4f core spectra were also analyzed. It should be noted that the presence of any A-site substituent cation or Bi deficiency in $BiFeO_3$ will be reflected in a slight shift in the binding energy of 4f core spectra.[27] In all samples Bi $4f_{7/2}$ and Bi $4f_{5/2}$ were observed at 158.9 eV and 164.2 eV, respectively, which matches well with the stoichiometric composition of $BiFeO_3$ suggesting that we have no Bi deficiency in these samples.

Optical properties reveal variation in the bandgap and changes in the prominent Fe *d-d* transitions that appear in the visible region. To study the bandgap and defect-related absorption characteristics, diffuse reflectance spectroscopy (DRS) was carried out at room temperature using a micro pack DH-2000 lamp (deuterium in UV-Vis and Halogen in Vis-NIR (visible near infrared)) and an Ocean Optics USB-2000 spectrometer. In DRS, scattered radiation is collected excluding specularly (normally) reflected light matching closely with the Kubelka-Munk function given by $F(R) = \frac{(1-R)^2}{2R}$, where R is the reflectance. The DRS data were collected with respect to a standard $BaSO_4$ reference. The absorbance *vs.* wavelength of samples with different crystallite sizes is shown in Fig. 4(a), and their reflectance was converted into the Kubelka-Munk function F(R). A plot of $[F(R)h\nu]^2$ vs. energy is shown in Fig. 4(b), where h is Plank's constant and ν is the frequency of illumination. The absorbance plots show a strong transition in the 500–600 nm range which corresponds to electronic transitions involving charge transfer from valence-band O 2p states to conduction-band Fe 3d states. This transition causes a blue shift with increasing particle size, with the absorption edge shifting from the higher wavelength side for BFO-5 to a lower wavelength side for BFO-65. The bandgap values, E_g, of $BiFeO_3$ nanoparticles, calculated using the Tauc relation: $(\alpha h\nu)^n \propto (h\nu - E_g)$ with $n = 2$ for direct bandgap, were plotted with respect to the particle size in Fig. 4(c). The bandgap shows a linear change from 2.13 eV for BFO-22 to 2.3 eV for BFO-38. For BFO-65, the bandgap is 2.32 eV which is still smaller than the bandgap values 2.5 to 2.8 eV reported for bulk $BiFeO_3$.[1,28] This *decrease* in bandgap with decreasing particle size is contrary to the more commonly observed increase in E_g with reduced particle size.[29]

The decrease in the bandgap value can be due to the existence of defect-induced energy levels between the conduction and valence bands, more specifically energy levels close to the conduction band. These shallow levels can reduce the effective bandgap for smaller particles, if their density is high. The presence of non-uniform microstrain in the particles modifies the energy levels, thereby influencing the absorption band edge.[30] In general, the microstrain in nanocrystallites is caused by several factors like non-uniform

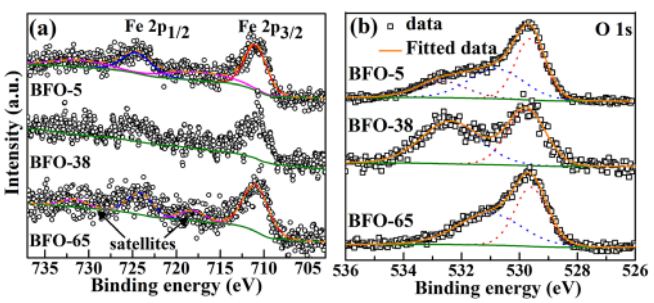

FIG. 3. (a) Fe 2p and (b) O 1s core shell x-ray photoelectron spectra of BFO-5, BFO-38, and BFO-65. Data are shown by open symbols with solid lines showing the overall fit for the data. Deconvoluted spectral peaks are shown as dotted lines. The Shirley background is also shown in the plots.

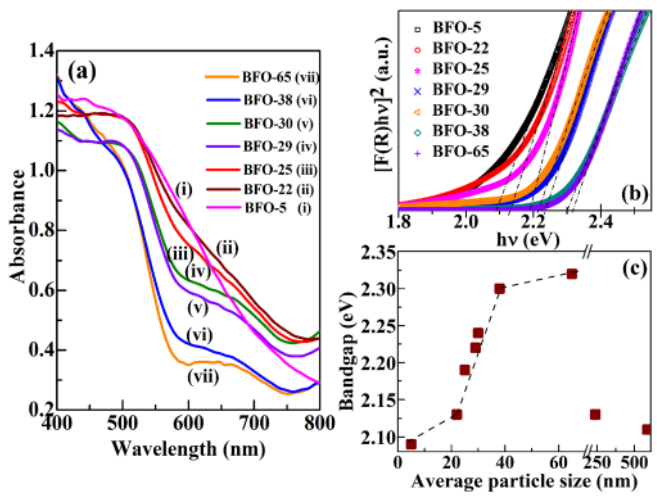

FIG. 4. (a) Absorbance versus wavelength measured from UV-vis diffuse reflectance spectra. The absorption edges at ~500 nm correspond to the charge transfer (CT) band. The broad band at ~650 nm corresponds to *d-d* transitions of Fe^{3+}. (b) $[F(R)h\nu]^2$ versus $h\nu$ plot of BFO nanoparticles. The intercept of the extrapolated absorption edge on the energy scale (x axis) gives the band gap of the samples. (c) The band gap estimated from (b) is plotted as a function of average crystallite size estimated from XRD.

lattice distortions, dislocations, antiphase domain boundaries, grain surface relaxation, etc. In $BiFeO_3$, the most common defects such as oxygen vacancies are major contributions to the microstrain. These oxygen vacancies reportedly lower than the adjacent Fe 3d levels, resulting in the sub-bandgap defect states.[31] Another contribution to the microstrain comes from the unsaturated bonds on the surface of the nanoparticles, which create deep and shallow levels within the bandgap.[32]

Significant differences in the bandgap values reported (varying between 2.5 and 2.8 eV) in the literature were shown to be influenced by several parameters including morphology, microstructure, chemical structure, and defects.[1] First-principle studies on the optical properties has shown that the absorption edge gets smoother and shifts to lower energy with increasing oxygen-vacancy concentration,[33] which is consistent with our observation on the shape of the absorbance curve which largely depends on defect concentration and microstrain in the material.

Contrary to the increasing trend in bandgap with increasing particle size till 65 nm, the bandgap reduces back to ~2.1 eV for larger particle sizes in the range 200–600 nm (Fig. 4 and supplementary material (Fig. S4)[24]). A similar trend of decreasing bandgap with increasing particle size (~400 nm) has been reported by Wang *et al.*[18] Such a fluctuation in band gap can be explained by considering how electron confinement, Coulomb interactions, and binding energy effects dominate each other in different particle size regimes.[1,34,35] The variation of bandgap within the range 65-200 nm could not be realized, as the fine control on particle size is limited by rapid growth of $BiFeO_3$ particle size with the increase in calcination temperature.

Optical bandgap in $BiFeO_3$ is also shown to decrease with increase in pressure or temperature.[1] This decrease in the bandgap with increase in the temperature has been attributed to the straightening of Fe-O-Fe bond angle,[36] which in turn changes the orbital overlap between the O 2p and Fe 3d levels.[37] At critical temperature (1024 K)[38] or pressure (50 GPa),[39] $BiFeO_3$ undergoes an insulator to metal transition with the optical bandgap falling to zero,[38] accompanied by a structural transition from orthorhombic (β) to cubic (γ) phase. It is noteworthy that the observed decrease in bandgap in the present study is also associated with a structural change (reduction in rhombohedral distortion) for particle sizes below 30 nm.

In addition to the strong absorption around 500–600 nm, a broad absorption band is seen between 600 and 700 nm (Fig. 4(a)). For bulk $BiFeO_3$, two distinct bands are reported around 600 nm and 750 nm corresponding to the *d-d* crystal field excitations of Fe^{3+} ions.[28] In the present case even for 65 nm sized $BiFeO_3$ nanoparticles, only a single broad band centered ~650 nm is seen. At smaller particle sizes, this broadening becomes much larger, and also the relative absorbance of this band with respect to charge transfer (CT) band grows higher. Such a broad absorption band with varying relative absorbance with respect to the CT band was also seen in $BiFeO_3$ with different morphologies reported by Li *et al.*[13] Qualitatively these changes can be attributed to the structural changes in $BiFeO_3$. As the size of the particles reduces, the linkage of FeO_6 octahedra across the unit cells is disturbed, altering the Fe-O-Fe distance.[33] This can affect the position and intensity of these bands.

In conclusion, a detailed study on the structural and optical properties of $BiFeO_3$ nanoparticles prepared by the sol-gel method was conducted. A control on the particle size introduces a systematic change in microstrain caused by oxygen defects in $BiFeO_3$ nanoparticles. XPS studies confirm that Fe is predominantly in the 3+ state and the presence of undercoordinated oxygen in smaller sized particles. A controlled change in bandgap values was demonstrated by merely controlling the calcination process, which in turn influences the particle size. Microstrain and oxygen defects were shown to exhibit a strong dependence on the particle size. This study suggests that microstrain, oxygen defects, and Coulombic interactions have a competing effect in determining the bandgap value of $BiFeO_3$ over a wide range of particle sizes; however, in a particular size regime, a systematic tuning of bandgap can be achieved by controlling the particle size. This approach provides the means of using bandgap-tuned $BiFeO_3$ nanoparticles for photovoltaic and photocatalytic applications.

The authors acknowledge the Boise State Center for Materials Characterization for TEM analysis. P.S.V.M. and C.S. acknowledge B. R. K. Nanda for useful discussion.

[1]G. Catalan and J. F. Scott, Adv. Mater. **21**(24), 2463–2485 (2009).
[2]G. Lawes and G. Srinivasan, J. Phys. D **44**(24), 243001 (2011).
[3]L. W. Martin, Y. H. Chu, and R. Ramesh, Mater. Sci. Eng. R: Rep. **68**(4–6), 89–133 (2010).
[4]T. Zhao, A. Scholl, F. Zavaliche, K. Lee, M. Barry, A. Doran, M. P. Cruz, Y. H. Chu, C. Ederer, N. A. Spaldin, R. R. Das, D. M. Kim, S. H. Baek, C. B. Eom, and R. Ramesh, Nat. Mater. **5**(10), 823–829 (2006).
[5]D. Lebeugle, D. Colson, A. Forget, M. Viret, A. M. Bataille, and A. Gukasov, Phys. Rev. Lett. **100**(22), 227602 (2008).
[6]S. H. Baek, H. W. Jang, C. M. Folkman, Y. L. Li, B. Winchester, J. X. Zhang, Q. He, Y. H. Chu, C. T. Nelson, M. S. Rzchowski, X. Q. Pan, R. Ramesh, L. Q. Chen, and C. B. Eom, Nat. Mater. **9**(4), 309–314 (2010).
[7]T.-J. Park, G. C. Papaefthymiou, A. J. Viescas, A. R. Moodenbaugh, and S. S. Wong, Nano Lett. **7**(3), 766–772 (2007).
[8]S. M. Selbach, T. Tybell, M.-A. Einarsrud, and T. Grande, Chem. Mater. **19**(26), 6478–6484 (2007).
[9]S. Y. Yang, L. W. Martin, S. J. Byrnes, T. E. Conry, S. R. Basu, D. Paran, L. Reichertz, J. Ihlefeld, C. Adamo, A. Melville, Y.-H. Chu, C.-H. Yang, J. L. Musfeldt, D. G. Schlom, J. W. Ager III, and R. Ramesh, Appl. Phys. Lett. **95**(6), 062909 (2009).
[10]U. A. Joshi, J. S. Jang, P. H. Borse, and J. S. Lee, Appl. Phys. Lett. **92**(24), 242106 (2008).
[11]F. Gao, X. Y. Chen, K. B. Yin, S. Dong, Z. F. Ren, F. Yuan, T. Yu, Z. G. Zou, and J. M. Liu, Adv. Mater. **19**(19), 2889–2892 (2007).
[12]T. Xian, H. Yang, J. F. Dai, Z. Q. Wei, J. Y. Ma, and W. J. Feng, Mater. Lett. **65**(11), 1573–1575 (2011).
[13]S. Li, Y.-H. Lin, B.-P. Zhang, Y. Wang, and C.-W. Nan, J. Phys. Chem. C **114**(7), 2903–2908 (2010).
[14]J. Kreisel, M. Alexe, and P. A. Thomas, Nat. Mater. **11**(4), 260 (2012).
[15]V. M. Fridkin, *Photoferroelectrics* (Springer London, Limited, 1979).
[16]J. Seidel, D. Fu, S.-Y. Yang, E. Alarcón-Lladó, J. Wu, R. Ramesh, and J. W. Ager III, Phys. Rev. Lett. **107**(12), 126805 (2011).
[17]S. Y. Yang, J. Seidel, S. J. Byrnes, P. Shafer, C. H. Yang, M. D. Rossell, P. Yu, Y. H. Chu, J. F. Scott, J. W. Ager, L. W. Martin, and R. Ramesh, Nat. Nanotechnol. **5**(2), 143–147 (2010).
[18]L. Wang, J.-B. Xu, B. Gao, A.-M. Chang, J. Chen, L. Bian, and C.-Y. Song, Mater. Res. Bull **48**(2), 383–388 (2013).
[19]F. Gao, Y. Yuan, K. F. Wang, X. Y. Chen, F. Chen, J.-M. Liu, and Z. F. Ren, Appl. Phys. Lett. **89**(10), 102506 (2006).
[20]A. Kumar, R. C. Rai, N. J. Podraza, S. Denev, M. Ramirez, Y.-H. Chu, L. W. Martin, J. Ihlefeld, T. Heeg, J. Schubert, D. G. Schlom, J. Orenstein,

R. Ramesh, R. W. Collins, J. L. Musfeldt, and V. Gopalan, Appl. Phys. Lett. **92**(12), 121915 (2008).
[21]R. Moubah, G. Schmerber, O. Rousseau, D. Colson, and M. Viret, Appl. Phys. Express **5**(3), 035802 (2012).
[22]G.-Q. Tan, Y.-Q. Zheng, H.-Y. Miao, A. Xia, and H.-J. Ren, J. Am. Ceram. Soc. **95**(1), 280–289 (2012).
[23]Y. Hu, L. Fei, Y. Zhang, J. Yuan, Y. Wang, and H. Gu, J. Nanomater. **2011** (2011).
[24]See supplementary material at http://dx.doi.org/10.1063/1.4813539 for XRD, bright-field and high-resolution TEM, and DRS for $BiFeO_3$ nanoparticles.
[25]C. Hammond, *The Basics of Crystallography and Diffraction* (Oxford University Press, Inc., New York, 2009).
[26]W. Qin, T. Nagase, Y. Umakoshi, and J. A. Szpunar, Philos. Mag. Lett. **88**(3), 169–179 (2008).
[27]Z. Quan, H. Hu, S. Xu, W. Liu, G. Fang, M. Li, and X. Zhao, J. Sol-Gel Sci. Technol. **48**(3), 261–266 (2008).
[28]B. Ramachandran, A. Dixit, R. Naik, G. Lawes, and M. S. R. Rao, Phys. Rev. B **82**(1), 012102 (2010).
[29]L. Brus, J. Phys. Chem. **90**(12), 2555–2560 (1986).
[30]A. M. Smith, A. M. Mohs, and S. Nie, Nat. Nanotechnol. **4**(1), 56–63 (2009).
[31]A. J. Hauser, J. Zhang, L. Mier, R. A. Ricciardo, P. M. Woodward, T. L. Gustafson, L. J. Brillson, and F. Y. Yang, Appl. Phys. Lett. **92**(22), 222901 (2008).
[32]K. Sattler, *Handbook of Thin Films* (Academic Press, San Diego, 2001), Vol. 5, pp. 61–97.
[33]S. Ju and T.-Y. Cai, Appl. Phys. Lett. **95**(23), 231906 (2009).
[34]Y. Kayanuma, Phys. Rev. B **38**(14), 9797–9805 (1988).
[35]Y. Nosaka, J. Phys. Chem. **95**(13), 5054–5058 (1991).
[36]A. Palewicz, R. Przeniosło, I. Sosnowska, and A. W. Hewat, Acta Crystallogr. **63**(4), 537–544 (2007).
[37]S. J. Clark and J. Robertson, Appl. Phys. Lett. **90**(13), 132903 (2007).
[38]R. Palai, R. S. Katiyar, H. Schmid, P. Tissot, S. J. Clark, J. Robertson, S. A. T. Redfern, G. Catalan, and J. F. Scott, Phys. Rev. B **77**(1), 014110 (2008).
[39]A. G. Gavriliuk, V. Struzhkin, I. S. Lyubutin, I. A. Trojan, M. Y. Hu, and P. Chow, in *MRS Online Proceedings Library*, 2006, Vol. 987.